

Lunar Penetrating Radar onboard the Chang'e-3 mission

Guang-You Fang, Bin Zhou, Yi-Cai Ji, Qun-Ying Zhang, Shao-Xiang Shen, Yu-Xi Li, Hong-Fei Guan, Chuan-Jun Tang, Yun-Ze Gao, Wei Lu, Sheng-Bo Ye, Hai-Dong Han, Jin Zheng and Shu-Zhi Wang

Institute of Electronics, Chinese Academy of Sciences, Beijing 100190, China;
gyfang@mail.ie.ac.cn

Received 2014 July 23; accepted 2014 September 29

Abstract Lunar Penetrating Radar (LPR) is one of the important scientific instruments onboard the Chang'e-3 spacecraft. Its scientific goals are the mapping of lunar regolith and detection of subsurface geologic structures. This paper describes the goals of the mission, as well as the basic principles, design, composition and achievements of the LPR. Finally, experiments on a glacier and the lunar surface are analyzed.

Key words: Chang'e-3 mission — moon rover — Lunar Penetrating Radar

1 INTRODUCTION

From the end of the 1950s to the end of the 1970s, the Soviet Union and the US space agency NASA launched many spacecrafts to the Moon, and some explorers successfully landed on the Moon (Heiken et al. 1991; Ouyang 2005). Since the end of the 1990s, the exploration of the Moon has again attracted attention because of its unknown origin and abundance of mineral resources. With the fast development of modern science, many novel technologies can be used to study and explore the Moon in detail. At present, the Moon's interior geological structure and the distribution of regolith thickness on the Moon are also poorly understood. If the thickness of lunar regolith can be measured, the content of mineral resources in the lunar regolith can be estimated. On the other hand, there is no overall understanding of the origin and formation process of the Moon. Due to geological structures on the Moon being related to its evolution history, if the geological conditions several kilometers beneath the Moon's surface can be explored, the origin and evolution of the Moon can be better understood.

Information about geological structures within a depth of 1–2 km in parts of the Moon have been known from the results of the US Apollo program. In 1973, the Apollo 17 spacecraft carried multi-band ground penetrating radar, which was named the Apollo Lunar Sounder Experiment (ALSE) (Porcello et al. 1974). ALSE operated in two HF bands (with center frequencies 5 MHz - HF1 and 15 MHz - HF2) and one VHF band (150 MHz), each with a bandwidth of 10% (using a chirped signal). The ALSE radar worked a total of 13 hours in lunar orbit and obtained many geological data to a depth of 1–2 km below the surface of the Moon. But due to limitations in electronic technology at that time, the radar has several shortcomings, mainly in the low quality and signal-to-noise ratio of the signal, no phase information, poor depth resolution and short detection time. For example, the depth resolution was about 150 m and the thickness distribution of lunar regolith could

not be detected. In addition, because the radar data were recorded on optical films, special pieces of equipment developed by NASA were needed to read the data, which lead to extreme difficulty in subsequent data processing. Up to now, NASA has only published some results from ALSE radar detected from some areas. From the published data, although ALSE radar was poor at discerning the composition and thickness of geological layers, these experimental results still provided important information for humans to better understand the Moon.

Japan developed a lunar spacecraft in the 1990s named Kaguya (SELENE). SELENE carried 14 scientific equipments, one of which was a Lunar Radar Sounder (LRS) which was used to detect geological structure at depths of 4–5 km under the surface of the Moon (Ono et al. 2010; Kobayashi et al. 2012). SELENE's LRS radar operated in the frequency range of 4 to 6 MHz, and a linear frequency-modulated pulse signal with a pulse width of 200 μ s and pulse power of 800 W were used. The power consumption and weight were respectively 50 W and 24 kg. The LRS system consists of two dipole antennas crossed each other. One dipole antenna is used to transmit the EM signals and both dipole antennas are used to receive the echo signals. SELENE was launched on 2007 September 14 with an orbital height of 100 km from the Moon. From 2007 November 20, LRS radar began to work. The LRS radar system obtained data about the geological structure from hundreds of meters to kilometers below the lunar surface, but its resolution was poor for identifying geological layers and it could not detect the thickness distribution of lunar regolith.

Both ALSE radar and LRS radar were installed on lunar orbiters, and they worked in a low frequency range with narrow bandwidth and poor resolution, which could not detect the thickness distribution of lunar regolith. This paper proposes an ultra-wideband ground penetrating radar mounted on a lunar rover to explore the thickness distribution of lunar regolith and geological structures of rock under the lunar surface, which was named Lunar Penetrating Radar (LPR) and is part of the Chang'e-3 (CE-3) mission (Ip et al. 2014). LPR is one of the important payloads on the CE-3 probe. This paper describes the working principle and scientific goals of LPR, and then summarizes the design of the radar system which includes the design technologies of the nanosecond pulse transmitter, nanosecond receiver and ultra-wideband antennas. Finally, the experimental results on the ground and on the Moon are given. The details of data processing and initial results of LPR can be found in a companion paper (Su et al. 2014). The performances of LPR onboard the rover of the CE-3 probe are evaluated based on results from a ground experiment (Zhang et al. 2014) and an echo simulation of LPR (Dai et al. 2014).

The plan of the paper is as follows. The next section presents the principle and scientific objectives of LPR. Section 3 describes of the LPR system. In this section, the operating techniques used by the LPR system, nanosecond pulse transmitters and receivers, ultra-broadband antennas are discussed. In Section 4, the experiment results on a glacier and the lunar surface are analyzed. A final conclusion is given in Section 5.

2 THE PRINCIPLE AND SCIENTIFIC OBJECTIVES OF LPR

LPR is a kind of nanosecond imaging radar that is carrier free and operates in the time domain. Its working principle is shown in Figure 1. It can be seen from the figure that the radar transmits a carrier free pulse signal into the lunar subsurface, and the pulse signal propagates into the lunar regolith and lunar crustal rock. If the pulse signal encounters an uneven layer, the interface of different media, rocks or other targets, it will be reflected and scattered back to the radar. By receiving the reflection and scattering signal and through data processing, analysis and inversion, the thickness and distribution of lunar regolith as well as the geological structure of the lunar subsurface along the rover's path can be detected.

The scientific objectives of the LPR are to complete the exploration of lunar subsurface structure along the path of the rover: (1) an exploration of thickness and layer structure in lunar regolith; (2) an exploration of geological structure in the shallow lunar crust.

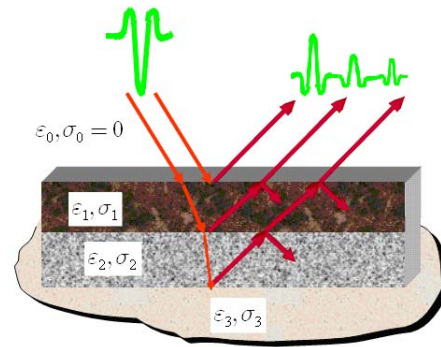


Fig. 1 Working principle of LPR.

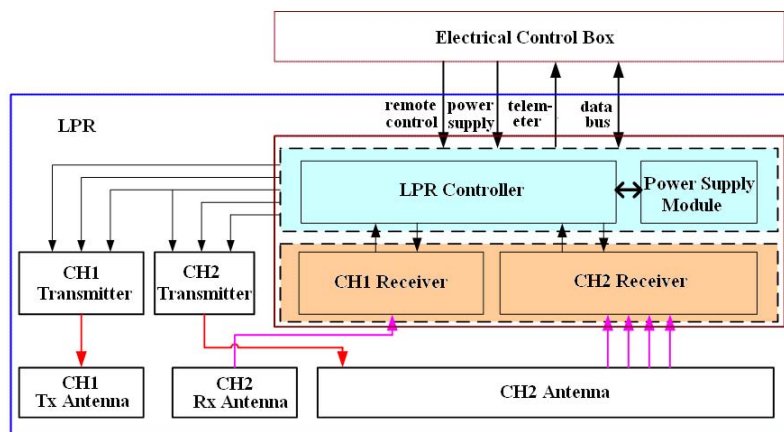


Fig. 2 Composition of the LPR system.

According to data measured by LPR, the following objectives of science and engineering research can be achieved: (1) to obtain the thickness distribution of lunar regolith along the path of the rover, and allow inversion of electromagnetic parameters describing lunar regolith and lunar shallow rocks to provide a basis for the estimation of mineral resources in the regolith; (2) to better understand the relationship between lunar terrain characteristics and geological structures, and provide scientific data for research on lunar morphological terrain and geology; (3) to provide a scientific basis for a detailed study of the formation and evolution of the Moon; (4) to provide necessary scientific data for the location of a future Moon base.

3 DESIGN OF THE LPR SYSTEM

In order to realize the scientific objectives, two detection channels are designed in the LPR system. The first channel (CH1) works in the frequency band 40–80 MHz and the depth resolution is about several meters. This channel is used to detect structure of the shallow lunar crust along path of the rover. The second channel (CH2) operates in the frequency band 250–750 MHz and the depth resolution is less than 30 cm. This channel is used to detect the thickness and structure of lunar regolith along the path of the rover. The composition of the radar system include the interface among

the internal parts, the interface between LPR and the electrical control box of the payload are shown in Figure 2.

As shown in Figure 2, the CH1 pulse transmitter is triggered by a clock signal from the LPR controller to generate a reliable pulse signal, and then the pulse is fed to the CH1 transmitting antenna and is transmitted into the lunar subsurface. The echo signal from the underground target is received by the CH1 receiving antenna and sent to the CH1 pulse receiver. The echo signal is amplified in the CH1 receiver which is controlled by the LPR controller, and then the amplified signal is sent to the controller for digitizing. According to the same principle, the CH2 completes the transmission and receives the pulse signal. All of the data from CH1 and CH2 are processed by the LPR controller and accumulated, and then the channel code and time code are inserted to the data, then the data are packed and sent to the integrated electronic system through the data bus.

3.1 Technique for Generating the Nanosecond Pulse

An avalanche transistor based on a Marx bank is usually used for generating a high voltage nanosecond pulse in the transmitter for ground penetrating radar (Daniels 2004). The transmitter includes four units, which are a trigger pulse generator unit, trigger pulse shaping unit, Marx bank and power supply. The trigger pulse generator unit is a digital integrated circuit which is used to generate a trigger pulse for the Marx bank. The trigger pulse shaping unit sharpens the trigger pulse. Several avalanche transistors are mounted as a cascade, charged in parallel and discharged in serial for a higher power narrow pulse in the Marx bank. Avalanche transistors in the Marx bank are biased near the maximum collector-base breakdown voltage $V_{(BR)CES}$ before the trigger pulse is initiated. When the trigger pulse is initiated, transistors are avalanched and higher power narrow pulses are generated with hundreds or even thousands of volts. The voltage is proportional to the number of avalanche transistors, and the width relies on the charging capacitor between every transistor. Low DC power is used by the trigger generator and pulse shaping units and higher DC power by the Marx bank, which are provided by the power supply unit.

Avalanche transistors often have a short lifetime because of the following reasons. The first reason is that avalanche transistors operate close to their avalanche breakdown voltage and have limited avalanche times. The imperfect static biasing will seriously affect the avalanche times. The second reason is that there is a large diversity in avalanche parameters, especially $V_{(BR)CES}$. The same circuit topology and static biasing will not apply to every transistor in the Marx bank. The circuit must be carefully designed. The third reason is that when the circuits operate at high voltage, high voltage will cause failure of components even if the average power is very small.

A highly reliable (which means long operating time) Marx-type nanosecond pulse generator is proposed in the LPR. The nanosecond pulse generator is shown in Figure 3. It consists of a trigger pulse generator, isolation circuit, Marx bank and power supply. The protection and isolation circuit between the trigger pulse generator and Marx bank ensure the safety of the trigger pulse generator. The bias voltage is defined through analysis, simulation and laboratory tests. An RF transformer with

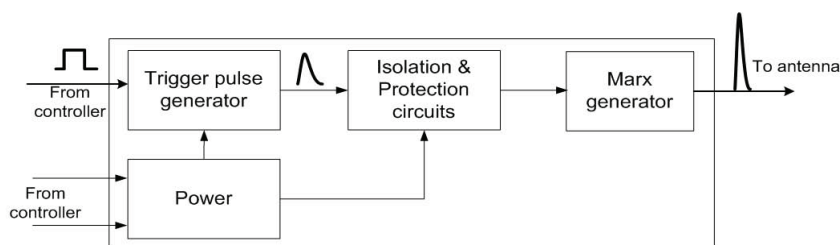


Fig. 3 Nanosecond pulse generator.

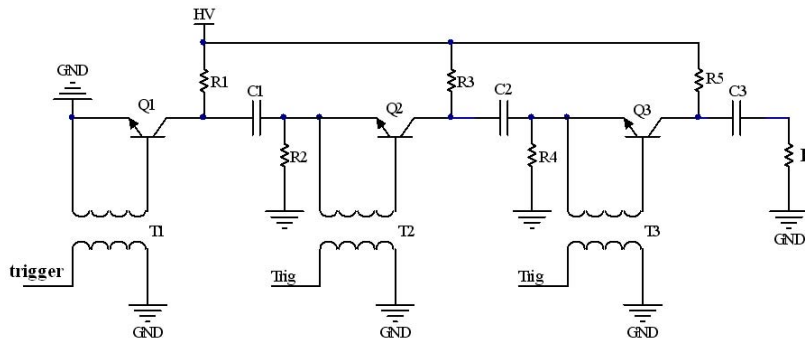


Fig. 4 The Marx bank circuit.

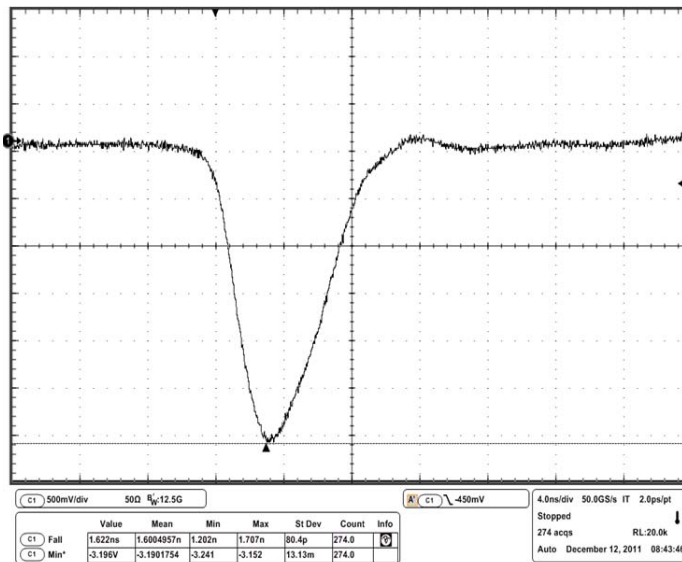


Fig. 5 Output pulse of the CH1 transmitter.

wide bandwidth feeds the trigger pulse to every transistor, as shown in Figure 4, and every transistor will breakdown at the same time and the reliability is enhanced. This nanosecond pulse transmitter has undergone all tests with no failures, and has been in service for over three months on the lunar surface with no failures.

Twelve avalanche transistors are incorporated in the Marx bank circuit in the transmitter for CH1, and produce a negative pulse. The peak amplitude of the negative pulse is 1033.45 V at a 50 Ω load with a 1.6 ns falling time. Ten avalanche transistors are included in the Marx bank circuit in the transmitter for CH2, and produce a balanced pulse. The peak amplitude of the balanced pulse is 398.2 V at a 100 Ω load with a 800 ps falling time. The output pulses for CH1 and CH2 are shown in Figures 5 and 6 respectively.

3.2 Technique for Receiving the Nanosecond Pulse

In time-domain ultra-wideband radar, the real-time sampling or equivalent-time sampling method can be used to receive the echo signal of the high-frequency nanosecond pulse. The real-time sam-

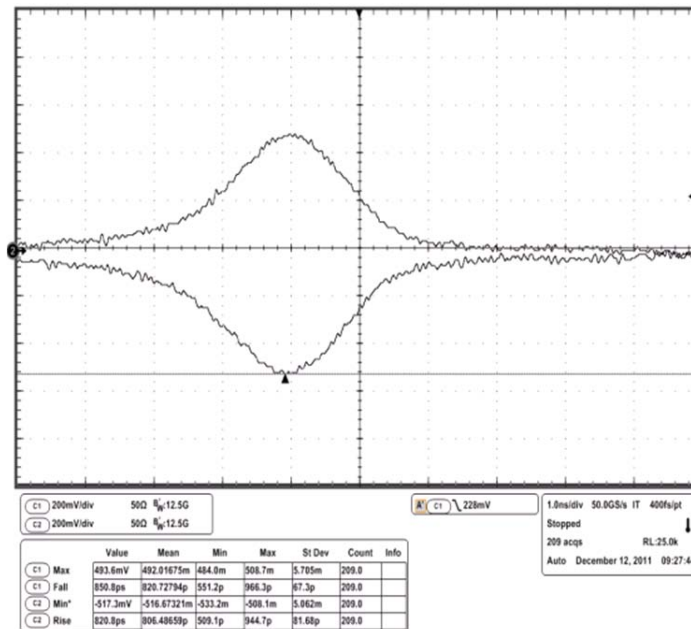


Fig. 6 Output pulse of the CH2 transmitter.

pling method uses a high-speed analog-to-digital converter (ADC) to digitize the echo signal, with the entire waveform being acquired by a single trigger. Due to the Nyquist sampling theorem and considering the time-domain ultra-wideband characteristics of the radar echo signal, the operating frequency of the ADC usually samples at 5~10 times the radar center frequency. The real-time sampling method has the advantages of a high utilization rate of echo and high radar scanning rate, but the disadvantages are the need for very high-speed ADC, high power consumption, difficulty in thermal design and complex storage and processing circuits to handle the high flow of output from the high-speed ADC. An equivalent-time sampling method utilizes multiple echo signals to reconstruct one equivalent waveform with frequency reduction or time-interleaved technology. A popular equivalent-time sampling method uses a diode bridge to reduce the repetitive high frequency signal to a low frequency signal which can be sampled by a low-speed ADC. The disadvantage of the popular equivalent-time sampling method is that a large number of echoes are often required to reconstruct one equivalent echo, and the echo utilization rate is low. Considering factors such as the center frequency of the radar, and availability and power consumption of the circuit components, a non-uniform quantization sampling technology based on 1-bit sampling quantization and gain control is adopted, so the LPR can have a higher rate when scanning for echoes and a larger dynamic range for receiving signals.

3.2.1 1-bit sampling technology

The block diagram of how 1-bit sampling technology operates is shown in Figure 7. The pulse echo signal is 1-bit that is sampled real-time and accumulated many times to achieve an equivalent 8-bit sampled waveform in the FPGA. The circuit is mainly composed of a high-speed comparator, a sampler and an 8-bit digital-analog converter (DAC). The amplified echo signal $V_g(t)$, which is biased to a specified voltage V_{g_DC} , is applied to the non-inverting input of the comparator. The output of the DAC V_{th} is applied to the inverting input of the comparator.

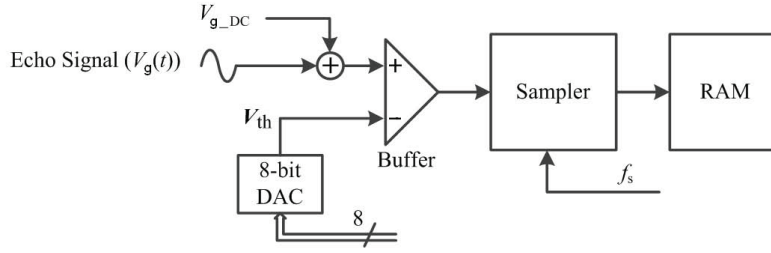


Fig. 7 Block diagram of 1-bit sampling.

The high speed digital signal output from the comparator is sampled at frequency f_s in the sampler. In a pulse repetition interval, the m -th sample output from the sampler, $S(m)$ is

$$S(m) = \begin{cases} 1 & \text{for } (V_g(t) + V_{g_DC}) > V_{th}, \\ 0 & \text{otherwise.} \end{cases} \quad (1)$$

As can be seen, the echo signal is sampled in real time in 1-bit and the sampling frequency is f_s . To achieve a higher quantization, the reference voltage at the inverting input of the comparator is changed as follows

$$V_{th}(n) = V_{init} + (n - 1)\Delta v, \quad n \in [1, 256], \quad (2)$$

where V_{init} is the initial reference voltage and Δv is the minimum voltage representing quantization. If the 1-bit sampling results are called $S_n(m)$ when the reference voltage is $V_{th}(n)$, after 256 repeated comparisons, the 256 sequences of 1-bit sampled results, $S_1(m) \sim S_{256}(m)$, can be expressed as a bitmap data matrix $B_{256 \times M}$

$$B_{256 \times M} = \begin{pmatrix} S_1(m) \\ S_2(m) \\ \vdots \\ S_{256}(m) \end{pmatrix}, \quad m \in [1, M]. \quad (3)$$

The m -th equivalent quantitative sample is $y(m)$

$$y(m) = \sum_{n=1}^{256} S_n(m). \quad (4)$$

The output produced by equivalent sampling is equivalent to the result which is directly acquired by using an 8-bit commercial ADC with sampling frequency f_s and minimum quantitative voltage Δv . The sampling frequency used by CH1 in LPR is 400 MHz and the sampling frequency used by CH2 in LPR is 3.2 GHz.

The 1-bit sampling technology used by LPR does not need a special high-speed ADC chip, which avoids the difficult requirement of space needed for a high-speed ADC device. The power consumption used by the radar system is also greatly reduced. In addition, the utilization rate of the echo has nothing to do with the sampling points. Rather, it is only associated with the total number of various reference voltages. Only 256 echo signals are needed to reconstruct the original signal waveform in 8-bit. The new equivalent sampling technique better utilizes energy in the echo signal compared with the traditional equivalent sampling technique when the number of sampling points is larger.

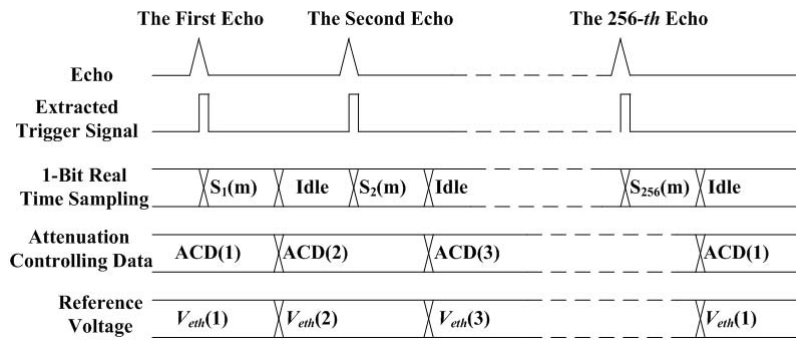


Fig. 8 Timing sequence diagram for sampling and gain control.

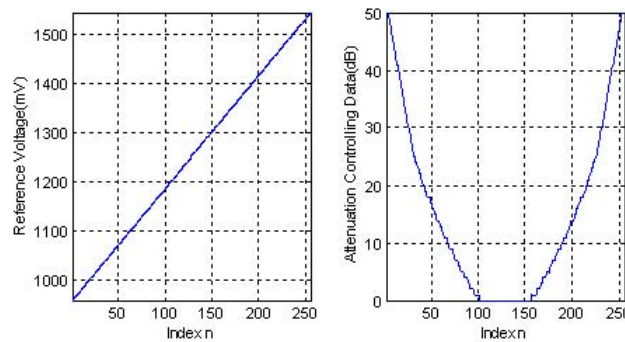


Fig. 9 Reference voltage curve corresponding to the RF attenuation.

3.2.2 Gain control method

The time-varying gain of the traditional gain control mode which applies gain to the signal in time is not suitable for the new equivalent sampling method that is adopted in the receiver of LPR, which is based on 1-bit real-time sampling technology. The amplitude-gain function is used to implement variable-gain control, namely the gain changes over a range of reference voltages, and a large gain will be used for a weak signal and a small gain will be used for a strong signal. The change in gain only needs to be completed in a pulse cycle, which greatly reduces the response time of the RF digital attenuator. The sampling and gain control timing of LPR is shown in Figure 8. The reference voltage curve corresponding to the RF attenuation is shown in Figure 9. By combining this kind of gain control method with 1-bit sampling technology, an equivalent 8-bit non-uniform quantization sampling technology can achieve a dynamic range of more than 90 dB.

3.3 Design of Ultra-broadband Antennas

The ultra-wideband antenna system is one of the most critical parts of the LPR system. The design requirements of the antenna system are mainly driven by scientific objectives of the exploration and its volume, weight and installation position on the lunar rover. LPR has two channels which are respectively connected to their own ultra-wideband antennas. The working frequency band of the CH1 antenna is 40–80 MHz and the working frequency band of the CH2 antenna is 250–750 MHz. As shown in Figure 10, two CH1 antennas are respectively mounted on two bottom sides of the top board of the moon rover, and are pointed toward the $-X$ direction. The CH2 antenna is mounted on

the bottom board of the lunar rover, and the main direction for radiation points toward the Moon's surface (in the $+Z$ direction).

3.3.1 Design of the CH1 antenna

According to the technical requirements of the CH1 antenna, considering the shape and size of the lunar rover and suitable locations for installation, two broadband monopoles grounded on the body of the lunar rover are chosen as the CH1 antennas. As shown in Figure 11, in order to facilitate the installation, the CH1 transmitting antenna and receiving antenna of LPR are respectively mounted on two bottom sides of the lunar rover's top board by an expansion mechanism. When the lunar rover arrives on the Moon, a command signal is sent from the ground base to release the mechanisms, and then the antennas are deployed along a specific track to the back of the lunar rover and directed toward the $-X$ direction, as shown in Figure 10.

Each of the CH1 antennas is mounted in a tubular radome. The radome is used to protect and support the monopole antenna. The radome is 1150 mm in length and 12 mm in diameter. The transmitting antenna and receiving antenna are spaced about 800 mm apart. In order to generate the pulse wave to propagate along the antenna without reflection, the Wu-King impedance loading method (Wu & King 1965) is used to load the antenna by a continuous resistive load from the feed point to the end of the antenna. In the actual process, the continuous distribution of the resistance load is generally difficult to produce, so a piecewise loading method which is shown in Figure 12 is usually used, namely concentrated resistive loading.

The Wu-King impedance loading method used for loading the antenna, and the antenna input impedance is designed to be $200\ \Omega$, thus a 1:4 impedance transformer is connected to the input port of the antenna in order to transform the antenna impedance from $200\ \Omega$ to $50\ \Omega$ and match the impedance of the feed cable. The FEKO software and FDTD method are employed to simulate and design the CH1 antenna, and the antenna prototypes are produced after the simulation and design. The antenna prototypes are installed on a prototype of the lunar rover, and the VSWR of the antenna was tested in an open space outdoors.

Figure 13 shows the VSWR characteristics of the CH1 antenna. As can be seen from the graph, the VSWR is less than 3 in the frequency band 40–80 MHz and the experimental results are in good agreement with the simulation results.

In order to test radiation patterns of the CH1 antennas, two 1:4 scale models of the CH1 antennas are produced and mounted on a 1:4 scale model of lunar rover. The 1:4 scale models of the CH1 antennas are unfolded and tested in an anechoic chamber. Figure 14 shows the normalized radiation patterns of the CH1 antenna. It can be seen that the H-plane radiation pattern of the CH1 antennas is approximately omnidirectional, and the simulation results and experimental results are in good agreement.

When the antenna is excited by a Gaussian pulse, the radiated pulse waveform 30 m away from the antenna is shown in Figure 15. It can be seen from the graph that the radiated pulse waveform from the CH1 antenna has less oscillation, which means that the antenna can meet the requirements of the LPR system.

3.3.2 Design of the CH2 antenna

A set of bow tie antennas is chosen as the CH2 transceiver antenna. In order to obtain ultra-wideband capability, the set of antennas is loaded by resistors in order to absorb the current reflected by the end of the set of antennas. In order to improve the radiation performance of the bow tie antennas and reduce interference from the surrounding environment, a shallow rectangular conducting cavity is added to the bow tie antennas. The cavity behind the antennas can increase radiation from the

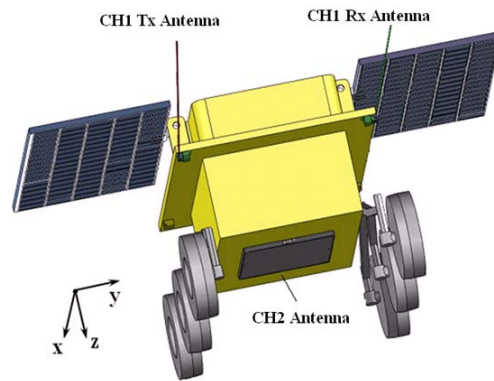


Fig. 10 Positions of the LPR antennas on the lunar rover.

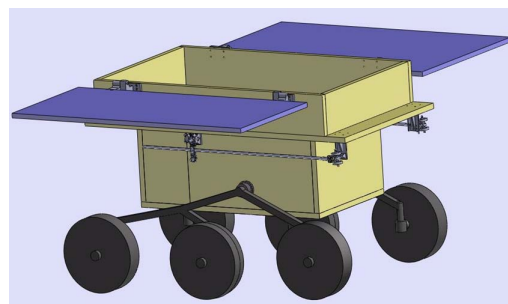


Fig. 11 CH1 antennas folded on the lunar rover.



Fig. 12 CH1 antenna loaded by piecewise resistors.

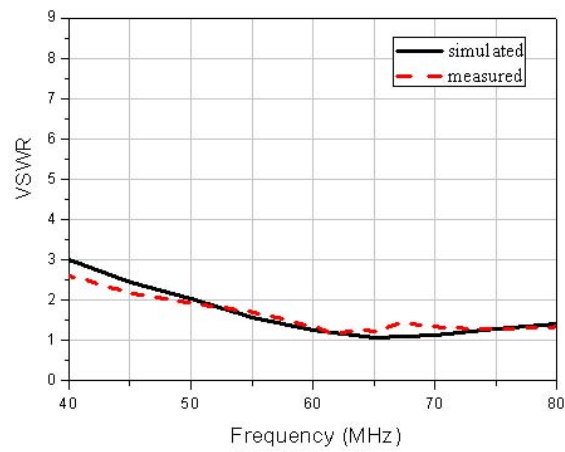


Fig. 13 VSWR of the CH1 antenna.

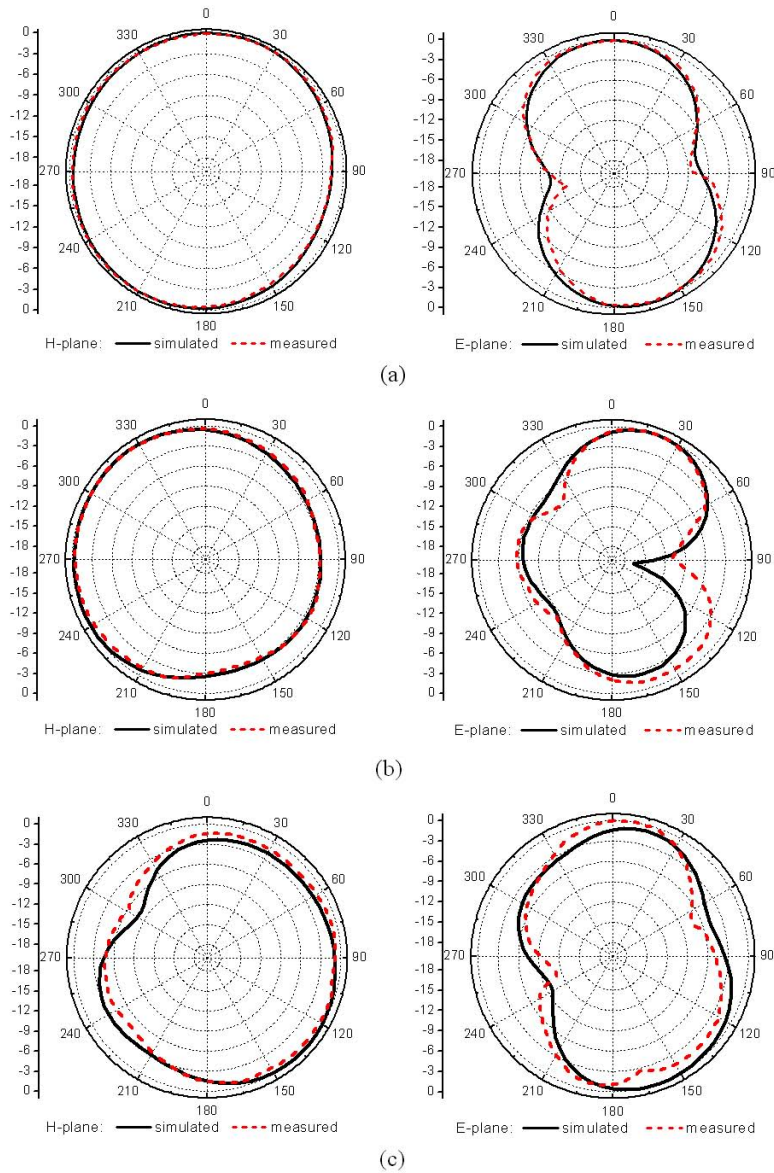


Fig. 14 Normalized radiation patterns of the CH1 antenna: (a) 40 MHz; (b) 60 MHz; (c) 80 MHz.

antennas directed toward the ground and provide a large forward to backward ratio (Vorobyov et al. 2007; Caratelli et al. 2009).

The CH2 transceiver antenna is mounted at the bottom of lunar rover, which is about 30 cm away from the ground. Figure 16 shows the structure of the CH2 antenna. As can be seen from the figure, the CH2 antenna has three antenna elements. The antenna elements are arranged side by side in a metal back cavity which is divided into three individual cavities. One antenna element is used to transmit EM waves and the other two are used to receive the EM waves. Each antenna element is 336 mm in length and 120 mm in width, and the space between the antenna elements is

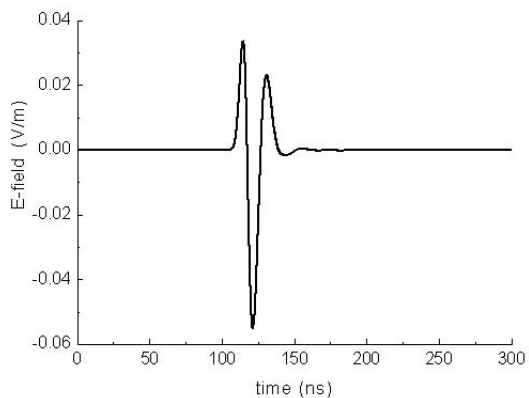


Fig. 15 The waveform of the electric field produced by the CH1 antenna.

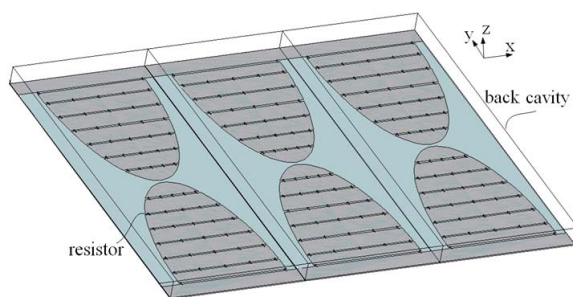


Fig. 16 The structure of CH2 antenna.

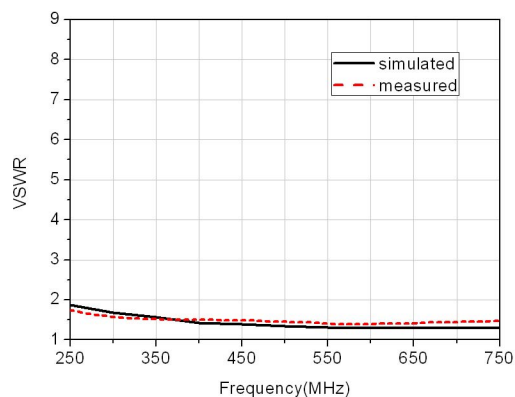


Fig. 17 VSWR of the CH2 antenna.

about 160 mm. The height of the back cavity of the antenna is reduced to 22 mm from a quarter of the center wavelength in order to ensure the lunar rover can maneuver over obstacles. In order to increase the bandwidth and improve the match between the antenna and the feed line, two identical half-ellipse shaped arms are used for the antenna element. The half-ellipse arm is divided into seven sections and loaded by five parallel resistors between each of the two subsections, which can decrease

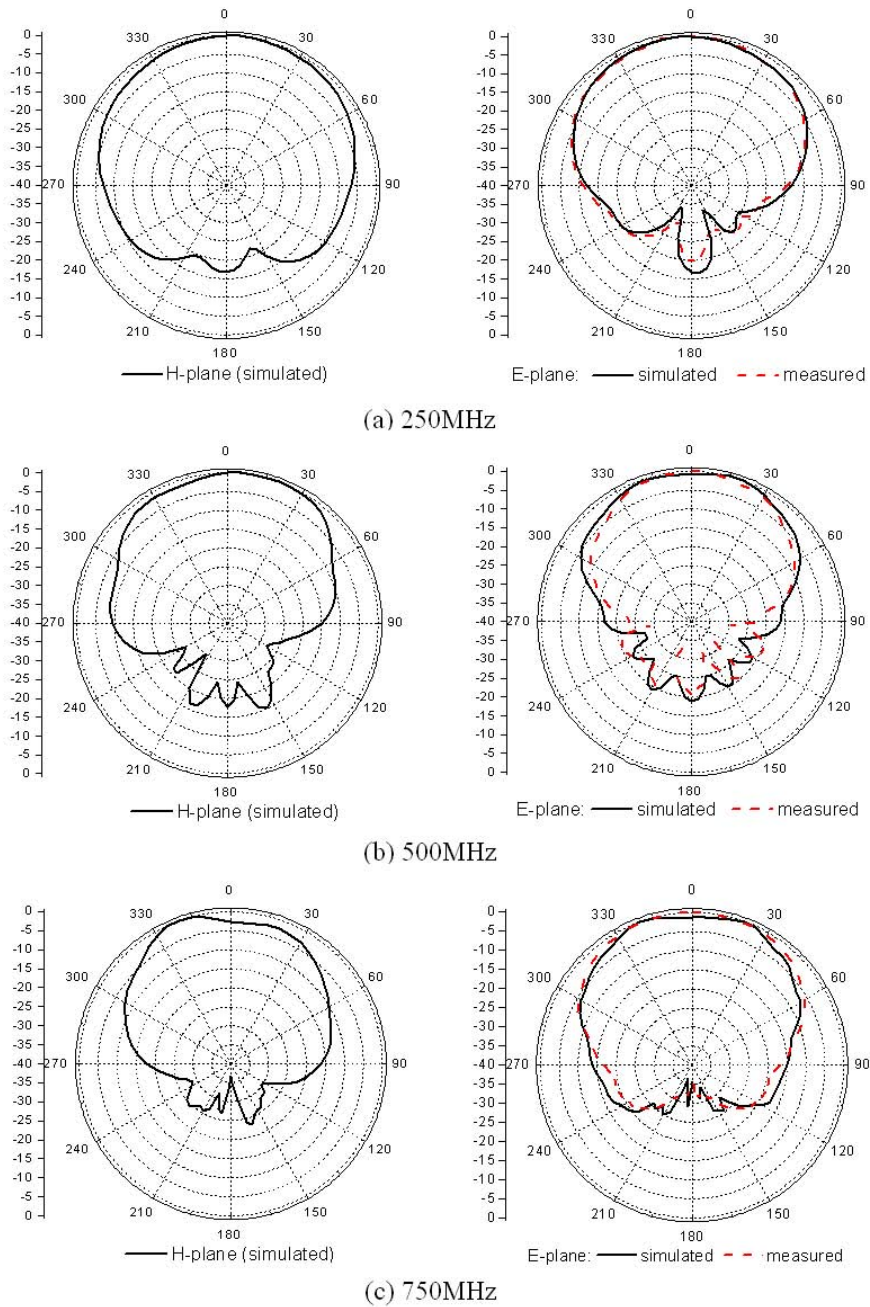


Fig. 18 Normalized far field radiation patterns of the CH2 antenna.

the reflections from the end of the arms. Both ends of the antenna element are connected to the back cavity by two respective parallel resistors. The input impedance of the antenna element is 100Ω and the antenna element is fed by a pair of parallel transmitting lines whose characteristic impedance is 100Ω .

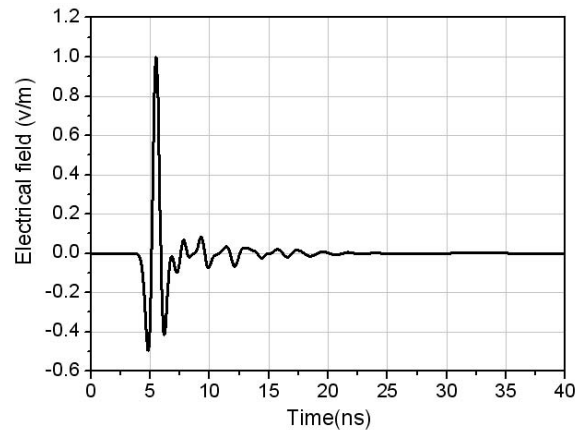


Fig. 19 Normalized waveforms of the electrical field produced by the CH2 antenna.

The CH2 antenna is simulated by FDTD and FEKO softwares. The antenna is manufactured and mounted on a prototype of the moon rover. Then its VSWR and radiation pattern are measured by a Vector Network Analyzer (Agilent E5071C) in an anechoic chamber. The antenna VSWR simulated by the FEKO software is shown in Figure 17. It can be seen that the VSWR is below 2.0 in the whole frequency range. Good agreements are achieved between the simulated results and the measured ones.

The normalized far field radiation patterns of E-plane and H-plane are simulated by the software FEKO and measured in an anechoic chamber. Figure 18 shows the simulated results and measured ones. It can be seen that the CH2 antenna has a smooth main lobe, good directivity, small backward radiation and the main radiation direction points to the ground. The simulated radiation pattern of the antenna is very consistent with the measured results. The simulated gain of the antenna is about -7 dBi at 500 MHz and the measured gain is about -7.5 dBi.

The radiated pulse waveform of the antenna in time domain is very important in the LPR system, which can directly affect the performance of the LPR system. The CH2 antenna is fed by a Gaussian pulse whose pulse width is about 2 ns. The normalized waveform of the radiated field 1 m away from the antenna is plotted in Figure 19. It is indicated that the antenna system has a good waveform in the time domain, which can satisfy the demands of the LPR system.

4 EXPERIMENTS ON THE GROUND AND LUNAR SURFACE

In order to evaluate the performance of LPR, the radar was tested on a dryland glacier in the Subei Mongol Autonomous County of Jiuquan City in Gansu province. The experimental results are shown in Figures 20 and 21. It can be seen from the figures that CH1 reached a depth of more than 150 m in the ice of the glacier, and CH2 reached a depth of more than 50 m in the ice of the glacier. The internal layers and bottom bedrock of the glacier can be clearly seen from radar images.

After the lunar rover landed on the Moon's surface, LPR started to work on 2013 December 15. A large amount of scientific data about exploring the lunar regolith and subsurface were successfully obtained. Figure 22 shows the shallow profile image of lunar regolith along the path of the lunar rover detected by CH2 on LPR. After preliminary analysis, CH1 can clearly detect information about the shallow layer of the lunar crust along the path of the lunar rover, and CH2 can clearly detect the layer structure of lunar regolith.

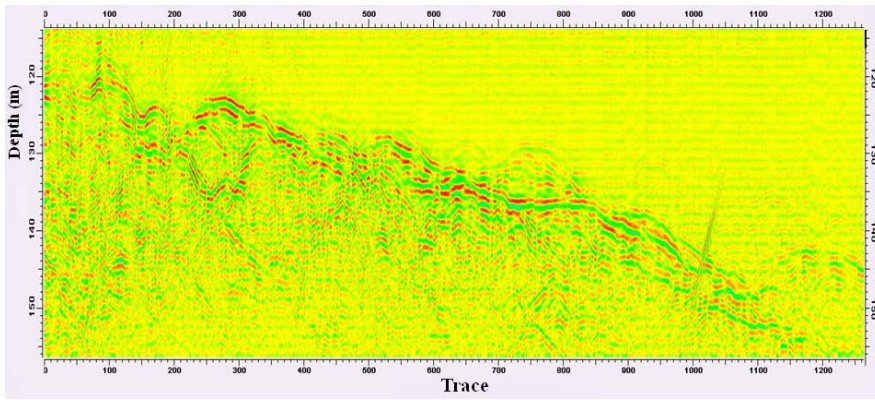


Fig. 20 LPR image of the glacier explored by CH1.

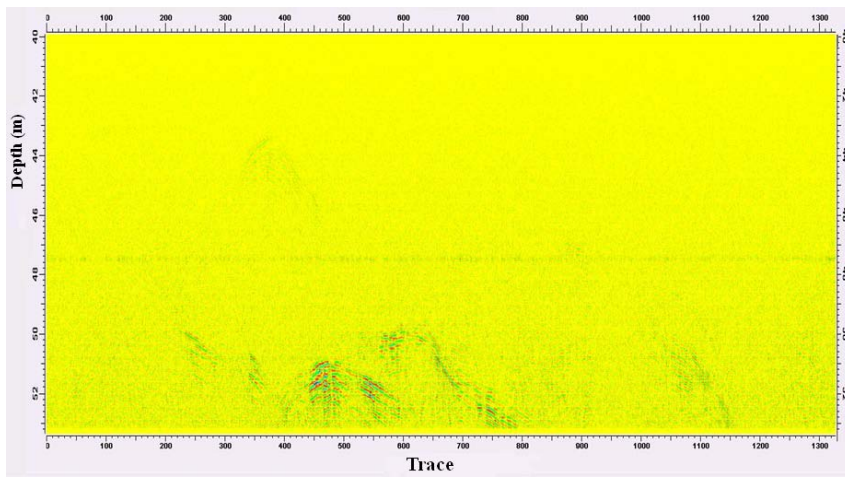


Fig. 21 LPR image of the glacier explored by CH2.

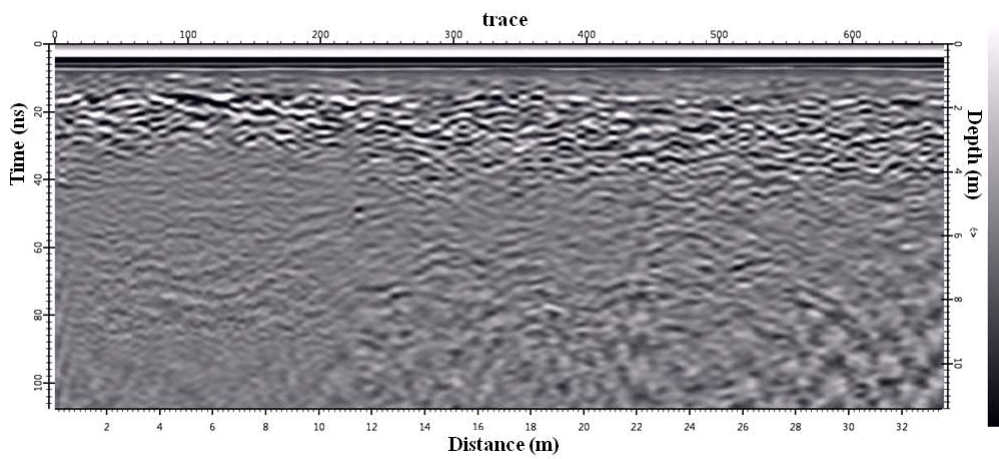


Fig. 22 LPR image of lunar regolith explored by CH2.

5 CONCLUSIONS

After more than five years of research, the LPR for the CE-3 mission was successfully developed at the Institute of Electronics, Chinese Academy of Sciences. On 2013 December 2, the CE-3 probe was successfully launched. After thirteen days of flight, the probe successfully landed on Mare Imbrium on 2013 December 14. LPR started to work on 2013 December 15. Many satisfying scientific data were acquired by LPR, and the design requirements of its engineering task were fulfilled.

Acknowledgements This work was funded by the second phase of the Chinese Lunar Exploration Program.

References

- Caratelli, D., Yarovoy, A., & Ligthart, L. P. 2009, *Antennas and Propagation, 2009. EuCAP 2009. 3rd European Conference on*, 2115
- Dai, S., Su, Y., Xiao, Y., et al. 2014, *RAA (Research in Astronomy and Astrophysics)*, 14, 1642
- Daniels, D. J. 2004, *Ground Penetrating Radar (London: The Institution of Engineering and Technology)*
- Ip, W.-H., Yan, J., Li, C.-L., & Ouyang, Z.-Y., 2014, *RAA (Research in Astronomy and Astrophysics)*, 14, 1511
- Heiken, G. H., Vaniman, D. T., & French, B. M. 1991, *Lunar Sourcebook - A User's Guide to the Moon (Cambridge: Cambridge Univ. Press)*
- Kobayashi, T., Lee, S. R., & Ping, J. S. 2012, in *Ground Penetrating Radar (GPR), 2012 14th International Conference on, IEEE*, 913
- Ono, T., Kumamoto, A., Kasahara, Y., et al. 2010, *Space Sci. Rev.*, 154, 145
- Ouyang, Z.-Y. 2005, *Introduction to Lunar Science (Beijing: China Astronautic Publishing House)*
- Porcello, L. J., Jordan, R. L., Zelenka, J. S., et al. 1974, *IEEE Proceedings, The Apollo Lunar Sounder Radar System*, 62, 769
- Su, Y., Fang, G.-Y., Feng, J.-Q., et al. 2014, *RAA (Research in Astronomy and Astrophysics)*, 14, 1623
- Vorobyov, A. V., Yarovoy, A. G., Aubry, P., & Ligthart, L. P. 2007, *Antennas and Propagation, 2007. EuCAP 2007. The Second European Conference on*, 1
- Wu, T., & King, R. 1965, *IEEE Transactions on Antennas and Propagation*, 13, 369
- Zhang, H.-B., Zheng, L., Su, Y., et al. 2014, *RAA (Research in Astronomy and Astrophysics)*, 14, 1633